Draft v1

October 22, 2010

Search for ν_ν to ν_e Oscillations in the MINOS Experiment

Tingjun Yang

(*for the MINOS collaboration*)

Stanford University[1]

E-mail: tjyang@fnal.gov

(Dated: October 22, 2010)

Abstract

The MINOS experiment uses the NuMI ν_μ beam to make precise measurements of neutrino flavor oscillations in the "atmospheric" neutrino sector. MINOS can also probe the yet unknown neutrino mixing angle θ_{13} by searching for a ν_e appearance signal in the ν_μ beam. This paper reviews the techniques developed for the first ν_e appearance analysis in MINOS.

[1] *Now at Fermi National Accelerator Laboratory, Batavia, IL, USA*

1 Introduction

Neutrinos have been a focus of experimental effort over the last decade. Many experiments have provided compelling evidence for neutrino flavor oscillations observed in measurements of neutrinos produced in the Sun, in the atmosphere, by accelerators, and by reactors [1–7]. The theoretical framework with which we describe the neutrino mixing has been well established. The three neutrino mass eigenstates, conventionally known as ν_1, ν_2, and ν_3 are related to the three flavor eigenstates ν_e, ν_μ, and ν_τ by the Pontecorvo-Maki-Nakagawa-Sakata (PMNS) matrix [9]. The PMNS matrix can be parameterized with 3 mixing angles, 1 CP violating phase δ_{CP}, and two Majorana phases if neutrinos are Majorana particles.

The present data require two large (θ_{12} and θ_{23}) mixing angles and one small (θ_{13}) mixing angle in the mixing matrix, and at least two independent mass squared differences, $\Delta m^2_{ij} \equiv m^2_i - m^2_j$ (where m_i's are the neutrino masses). Δm^2_{21} and θ_{12} drive the solar neutrino oscillations while $|\Delta m^2_{31}|$ and θ_{23} drive the atmospheric neutrino oscillations. These parameters are relatively well determined [1, 5–7]. However, only an upper bound is derived for the mixing angle θ_{13} and barely nothing is known on the CP phase δ_{CP} and on the sign of Δm^2_{31}. Since the two mixing angles θ_{12} and θ_{23} are known to be relatively large, a non-zero value of θ_{13} would open the possibility of observing CP violation in the leptonic sector. Also a non-zero θ_{13} is important for the determination of the neutrino mass ordering. For these reasons, it is a main objective of upcoming reactor and accelerator experiments to directly measure this parameter.

The MINOS experiment uses a beam of muon neutrinos to make precise measurements of neutrino oscillations in the "atmospheric" neutrino sector. MINOS has made the most

precise measurement of the atmospheric mass splitting $|\Delta m^2| = (2.43 \pm 0.13) \times 10^{-3}$ eV^2 by measuring the disappearance of muon neutrinos [7, 8]. At this mass scale, the dominant oscillation channel is expected to be $\nu_\mu \rightarrow \nu_\tau$; however the sub-dominant $\nu_\mu \rightarrow \nu_e$ transition mode is not excluded [1]. Observation of this transition mode would indicate a non-zero value of the yet unknown mixing angle θ_{13}. The most stringent constraint on θ_{13}, obtained by the CHOOZ reactor experiment [10], implies $\sin^2(2\theta_{13}) < 0.15$ at the 90% C.L. for the value of $|\Delta m^2|$ measured by MINOS. MINOS is the first experiment to probe θ_{13} with sensitivity beyond the CHOOZ limit. In this paper, we will review some of the key techniques developed for the first MINOS ν_e appearance analysis based on 3.14×10^{20} protons on target (POT) [11]. Most of the techniques discussed in this paper were also applied to the updated analysis based on 7.01×10^{20} POT [12]. We will briefly discuss the updated analysis in the end.

2 The MINOS Experiment

MINOS is a long baseline accelerator neutrino experiment. A beam of muon neutrinos are produced in the Fermilab accelerator (NuMI facility) [13]. Protons of 120 GeV are extracted from the Main Injector accelerator and focused onto a rectangular graphite production target. The particles produced in the target are focused (one sign only) by two magnetic horns. The neutrino beam is produced from secondary pion and kaon decays in the decay pipe. The horn current and the position of the target relative to the horns can be configured to produce different neutrino energy spectra. In the standard low energy configuration optimized for the oscillation studies, the neutrino beam is peaked at 3 GeV and the beam composition is 98.7% ν_μ and $\bar{\nu}_\mu$, and 1.3% ν_e and $\bar{\nu}_e$. The neutrinos are observed in two detectors: a

Near Detector (ND) 1 km from the production target and a Far Detector (FD) 735 km from the target. Both detectors are tracking calorimeters composed of planes of 2.54 cm thick steel and 1.0 cm thick scintillator (with a sampling frequency of 1.4 radiation lengths per plane). The scintillator planes are segmented into 4.1 cm wide strips which corresponds to 1.1 Molierè radii [14].

The data used for the first ν_e analysis were recorded between May 2005 and July 2007, corresponding to an exposure of 3.14×10^{20} POT. The Monte Carlo (MC) simulation of the beam line and the detector is based on GEANT3 [17] and the hadron production yields from the target are based on FLUKA [18]. Neutrino interactions and further rescattering of the resulting hadrons within the nucleus are simulated using NEUGEN3 [19]. The hadnization model [20], important for the simulation of shower topology in the MINOS detector, employs a KNO-based empirical model [21] for the low invariant mass interactions and PYTHIA [22] for the high invariant mass interactions.

3 Electron Neutrino Identification

The signature of $\nu_\mu \rightarrow \nu_e$ transition is an excess of ν_e-induced charged-current (CC) events. The sensitivity of the MINOS $\nu_\mu \rightarrow \nu_e$ oscillations analysis depends on the separation of the signal ν_e-CC events from background events. The selection algorithm identifies the short and narrow shower that is consistent with an electromagnetic cascade in the MINOS calorimeter. The dominant background is the π^0 produced via neutral-current (NC) interaction or via ν_μ-CC interaction with a short muon track. An irreducible ν_e background arises from the 1.3% ν_e and $\bar{\nu}_e$ component of the beam. This beam ν_e background results primarily from

secondary muon and kaon decays. The ν_e selection cuts preferentially select low energy beam ν_e events which result primarily from μ^+ decays. Since μ^+ is mainly the decay product of the π^+ decays, and we constrain π^+ production at target well by the measured ν_μ-CC spectrum, the systematic uncertainty on the predicted beam ν_e background is small. A smaller background component arises from the cosmogenic sources. In the Far Detector, there is additional background source: ν_τ from $\nu_\mu \rightarrow \nu_\tau$ oscillations followed by $\tau \rightarrow e/\pi^0$ decays.

The data events are required to have been recorded while the detector was fully operational. Selection criteria are applied to select signal events and suppress background events. Cosmogenic backgrounds in this analysis are reduced to less than 0.5 events (90% C.L.) in the FD by applying directional requirements and requiring the events to be in time with the accelerator pulse. Selected events must have reconstructed energy between 1 and 8 GeV. The low energy cut removes mainly NC backgrounds, while the high energy cut removes high energy beam ν_e backgrounds resulting from kaon decays. To remove the poorly reconstructed events, selected events are required to have a reconstructed shower and at least 5 contiguous planes, each with energy depositions above half the energy deposited by a minimum ionizing particle. Events with long tracks are rejected to remove ν_μ-CC backgrounds. The signal to background ratio in the FD improves from 1:55 to 1:12 after applying these loose cuts assuming θ_{13} is at the CHOOZ bound.

Further enhancement of signal over background ratio is achieved using an artificial neural network (ANN) with 11 input variables characterizing the longitudinal and transverse energy deposition in the calorimeter [23]. Some of the variables are parameters characterizing the longitudinal shower profile, energy fraction in windows of 2, 4 or 6 planes, fraction of energy

in a 3-strip wide road, RMS of the transverse energy deposition, *etc.* The architecture of the neural network is optimized to consist of two hidden layers, each consisting of 6 nodes. Maximum sensitivity is achieved by selecting events with the neural network output above 0.7. This acceptance threshold is determined by maximizing the ratio of the accepted signal to the expected statistical and systematic uncertainty of the background. Figure 1 shows the ANN output distributions for simulated FD signal and background events. This method give a 1:3 signal-to-background ratio assuming θ_{13} is at the CHOOZ bound and after making data driven corrections to the background estimation.

4 ND Background Decomposition

In order to obtain the optimal sensitivity on θ_{13}, it is crucial to have an accurate estimate of the background yield in the ν_e appearance analysis. The FD background prediction is obtained through extrapolation from the ND in individual reconstructed energy bins:

$$(FD)^{Prediction} = (ND)^{Data} \times (F/N)^{MC}, \tag{1}$$

i.e. the background rate is measured in the ND and then multiplied by the Far/Near ratio calculated using MC to get the FD background prediction. The Far/Near ratio is robust since a lot of systematic effects cancel to a large extent. In practice, however, the extrapolation to the FD is complex because different background sources extrapolate differently. The ν_μ-CC background is suppressed in the FD because of $\nu_\mu \rightarrow \nu_\tau$ oscillations while the NC background is unaffected by the oscillations. Also the muons tend to decay further

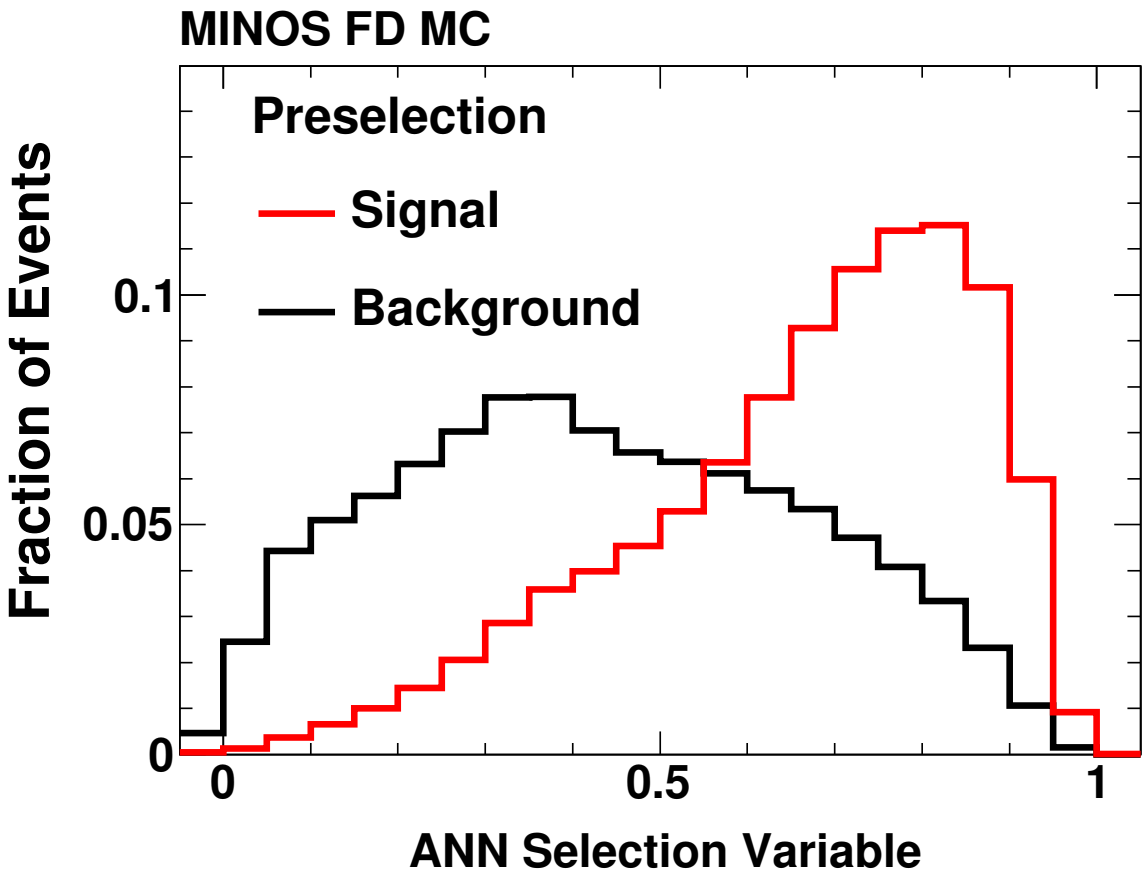

Figure 1: The ANN output distributions for simulated FD signal and background events. The following oscillation parameters are used: $\sin^2(2\theta_{13}) = 0.15$, $|\Delta m^2| = 2.43 \times 10^3$ eV^2, and $\sin^2(2\theta_{23}) = 1$.

downstream in the decay pipe and the resulting beam ν_e spectra are slightly different at the two detectors because of different detector solid angles. The extrapolation of each of the primary background components is treated separately and some knowledge about the relative contribution from different background sources is necessary.

The ND background components are determined from comparison of background rates in two different beam configurations. The first configuration is the standard one used for the appearance search. In the second configuration, the current in the focusing horns is turned off so no hadrons are focused. Consequently, the low-energy peak of the neutrino energy distribution disappears, and the selected event sample is dominated by NC events from higher energy neutrino interactions. These two configurations give significantly different ratios of ν_μ-CC to NC background rates and thus a comparison of background levels can yield information regarding relative contributions from these two sources. The total background in each reconstructed energy bin can be written as a sum of the individual components:

$$N^{on} = N_{CC} + N_{NC} + N_{b\nu_e} \quad (2)$$

$$N^{off} = r_{CC} \cdot N_{CC} + r_{NC} \cdot N_{NC} + r_{b\nu_e} \cdot N_{b\nu_e} \quad (3)$$

where

$$r_{CC} = \frac{N_{CC}^{off}}{N_{CC}}, r_{NC} = \frac{N_{NC}^{off}}{N_{NC}}, r_{b\nu_e} = \frac{N_{b\nu_e}^{off}}{N_{b\nu_e}}, \quad (4)$$

N^{on} and N^{off} are the numbers of data events selected as ν_e candidates obtained in the above two configurations, and $N_{CC}^{(off)}$, $N_{NC}^{(off)}$, $N_{b\nu_e}^{(off)}$ are the simulated background ratios when the horns are turned on (off). The ratios of rates (4) in the two beam configurations for each

background component are well modeled because of the cancellation of systematic effects and hence are taken from MC simulation and used as inputs for this method. The beam ν_e background component is also taken from MC simulation since it is well constrained by the ND ν_μ-CC data. Eqs (2) and (3) can be solved in reconstructed energy bins to obtain the ν_μ-CC and NC background spectra. Figure 2 shows the energy spectrum measured in the ND for events passing the ν_e selection criteria and the extracted NC, ν_μ-CC, and beam ν_e components. The ND background is (57±5)% NC, (32±7)% ν_μ-CC, and (11±3)% beam ν_e events. The errors on the components are derived primarily from the data and are correlated due to the constraint that the background must add up to the observed ND event rate. This constraint also leads to a much reduced error on the FD background prediction.

A second decomposition technique was applied to verify the background components. This method uses identified ν_μ-CC events with the muon track removed. The remnant hits are expected to imitate the NC-induced showers. This sample is used to correct the simulated selection efficiency for the NC events. This second method yields consistent ND background components [24, 25].

5 FD Background and Signal Predictions

After decomposition of the ND data into separate background components, each spectrum is multiplied by the Far to Near energy spectrum ratio from the simulation for that component, providing a prediction of the FD background spectrum. $\nu_\mu \rightarrow \nu_\tau$ oscillations are included when predicting the FD event rate. We expect 26.6 background events, of which 18.2 are NC, 5.1 are ν_μ-CC, 2.2 are beam ν_e and 1.1 are ν_τ.

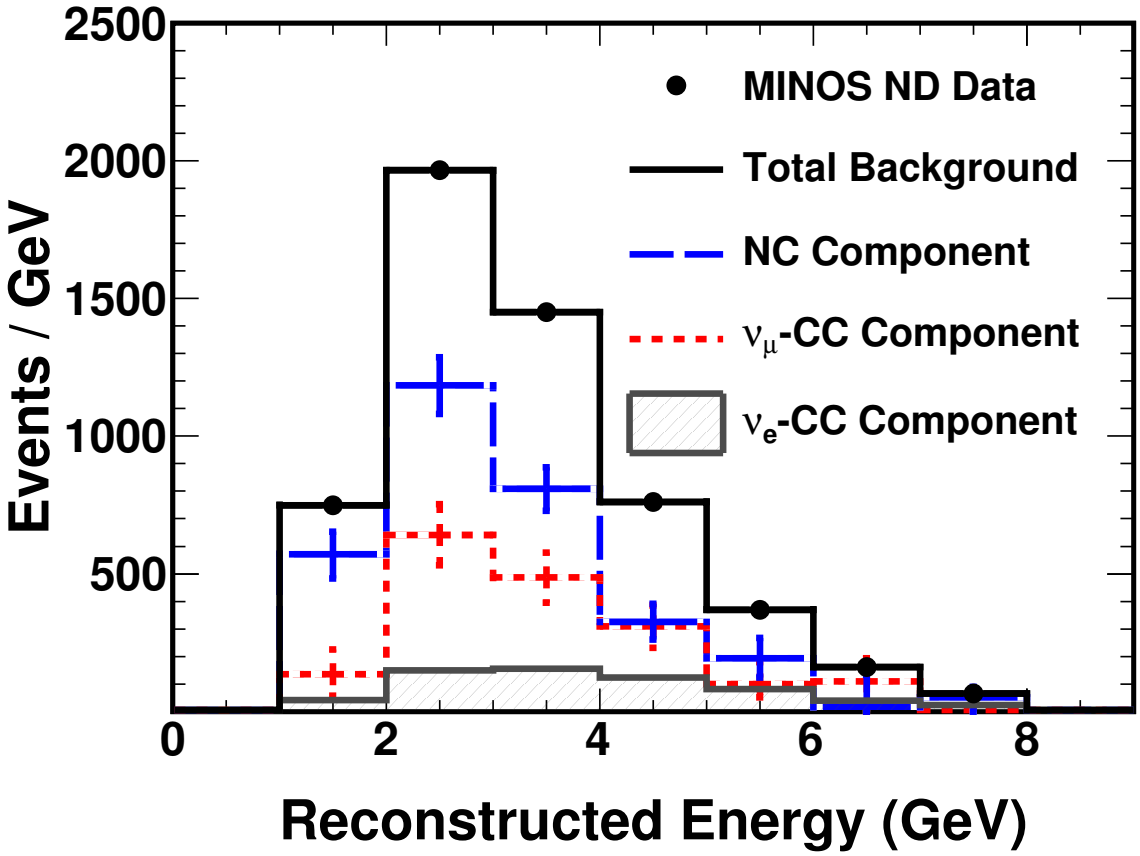

Figure 2: Reconstructed ND energy spectra of the ν_e selected backgrounds from NC (dashed) and ν_μ-CC (dotted) interactions as obtained from the horn-off method. The shaded histogram shows the beam ν_e component from the simulation. The solid histogram corresponds to the total of these three components which are constrained to agree with the data points. The statistical uncertainties on the data are negligible and are invisible on this scale; uncertainties on the components are systematic.

Systematic uncertainties are evaluated by generating MC samples with systematic effects varied over their expected range of uncertainty and quantifying the change in the number of predicted background events in the FD. Most of the dominant uncertainties arise from Far/Near differences.

One effect that has a large impact on the background prediction is the photo-multiplier tube (PMT) crosstalk modeling. It was discovered in the early stage of the ν_e analysis that the low pulse-height hits had a rather large impact on the shower topology and consequently the ν_e identification algorithm. We identified PMT crosstalk as one of the biggest contributors to the low pulse-height hits. The crosstalk phenomenon is an inherent property for multi-anode PMTs. Approximately 7% of the signal from light on a given pixel may appear in neighboring pixels. The MINOS detector readout system uses Hamamatsu 64-anode (M64) PMTs for the ND [15] and 16-anode (M16) PMTs for the FD [16]. This can be a source of Far/Near differences. The crosstalk was imperfectly modeled in the initial version of the MC used in this analysis. We used the cosmic ray data to improve the crosstalk simulation. Figure 3 shows the average crosstalk charge as a function of the deposited charge between two neighboring pixels of the M64 PMT before and after the tuning using cosmic ray data. A much improved simulation was achieved after the tuning. Based on these studies, we decided to remove low pulse-height hits when constructing the ANN input variables so as to make the MINOS ν_e analysis insensitive to any inaccuracies in the crosstalk modeling and generate a small sample of MC with improved crosstalk simulation to evaluate the systematic effect. The improved crosstalk modeling was used in the MC simulation for the updated MINOS ν_e analysis based on 7.01×10^{20} POT.

Table 1 shows that the uncertainty in the total number of background events in the

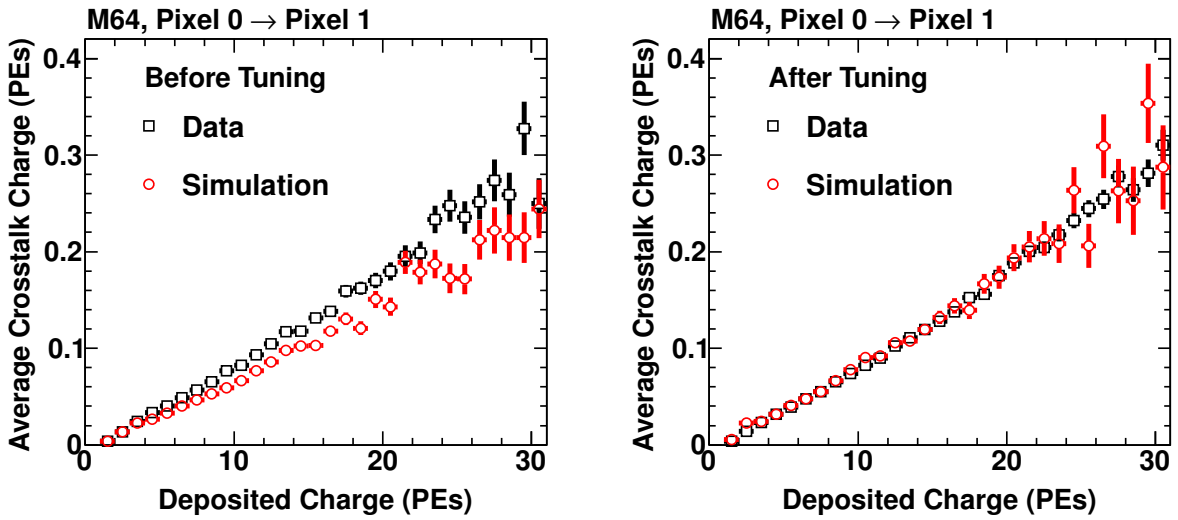

Figure 3: Average crosstalk charge appeared in Pixel 1 as a function of charge deposited in Pixel 0 for the M64 PMT measured using the cosmic ray data. Pixel 0 and Pixel 1 are neighboring pixels between which crosstalk is most prominent. The charge is measured in photo-electrons. The left plot shows the comparison of data and simulation before the crosstalk tuning where the simulation underestimates the crosstalk fraction. The right plot shows the improved agreement after the tuning. The two data distributions are not identical because the two samples have different numbers of cosmic ray muon tracks and the new sample is reconstructed with improved reconstruction software and calibration constants.

Far Detector. The dominant uncertainties arise from Far/Near differences: relative energy scale calibration differences, details of the modeling of the PMT gains and crosstalk, and relative event rate normalization. Other uncertainties resulting from neutrino interaction physics, shower hadronization, intranuclear rescattering, and absolute energy scale uncertainties affect the events in both detectors in a similar manner and mostly cancel in the extrapolation. The use of the same materials and detector segmentation in the ND and FD is critical in achieving this error cancellation. The individual systematic errors on the expected background are combined in quadrature with the uncertainty from the decomposition of the background to give an overall systematic uncertainty of 7.3% on the expected number of background events in the FD.

To estimate the efficiency for selecting ν_e-CC events, we use a sample of showers from ν_μ-CC events selected with long tracks. The hits associated with the muon track are removed from the events, and then a simulated electron of the same momentum as the removed muon is embedded in the remnant showers. Test beam measurements indicate that the selection efficiency of single electrons is well described by the simulation. We compare the ν_e-CC selection efficiencies evaluated using the muon-removed events from data and MC. The selection efficiency obtained from the data agrees with that obtained from the MC to within 0.3%. The difference is applied as a correction factor to correct the simulated ν_e-CC selection efficiency. We also evaluate the systematic uncertainties on the correction factor. We estimate our signal selection efficiency to be (41.4$\pm$1.5)% [24].

Uncertainty source		Uncertainty on background events
Far/Near ratio:		6.4%
(a) Relative Energy Scale	3.1%	
(b) PMT Gains	2.7%	
(c) PMT Crosstalk	2.2%	
(d) Relative Event Rate	2.4%	
(e) All Others	3.7%	
Horn-off		3.5%
Total Systematic Uncertainty		7.3%

Table 1: Systematic uncertainty in the total number of background events in the Far Detector.

6 Results

We examined the FD data after we finalized the background estimation and the signal selection efficiency. Figure 4 shows the number of selected candidate events in the FD as a function of the ANN selection variable. In the signal region where the ANN selection variable is greater than 0.7, we observe 35 events with a background expectation of 27±5(stat)±2(syst), a 1.5 σ excess over the expected background.

Figure 5(a) shows the values of $\sin^2(2\theta_{13})$ and δ_{CP} that give a number of events consistent with our observation for 3.14×10^{20} POT. The oscillation probability is computed using a full 3-flavor neutrino mixing framework with matter effects, which introduces a dependence on the neutrino mass hierarchy (the sign of Δm^2). The MINOS best fit values of $|\Delta m^2| = 2.43 \times 10^{-3}$ eV^2 and $\sin^2(2\theta_{23}) = 1.0$ are used as constants in the calculation. Statistical and systematic uncertainties are included when constructing the confidence intervals via the Feldman-Cousins approach. Interpreted as an upper limit on the probability of $\nu_\mu \rightarrow \nu_e$ oscillations, the 3.14×10^{20} POT data set requires $\sin^2(2\theta_{13}) < 0.29$ (0.42) at the 90% C.L. at $\delta_{CP} = 0$ for the normal (inverted) hierarchy.

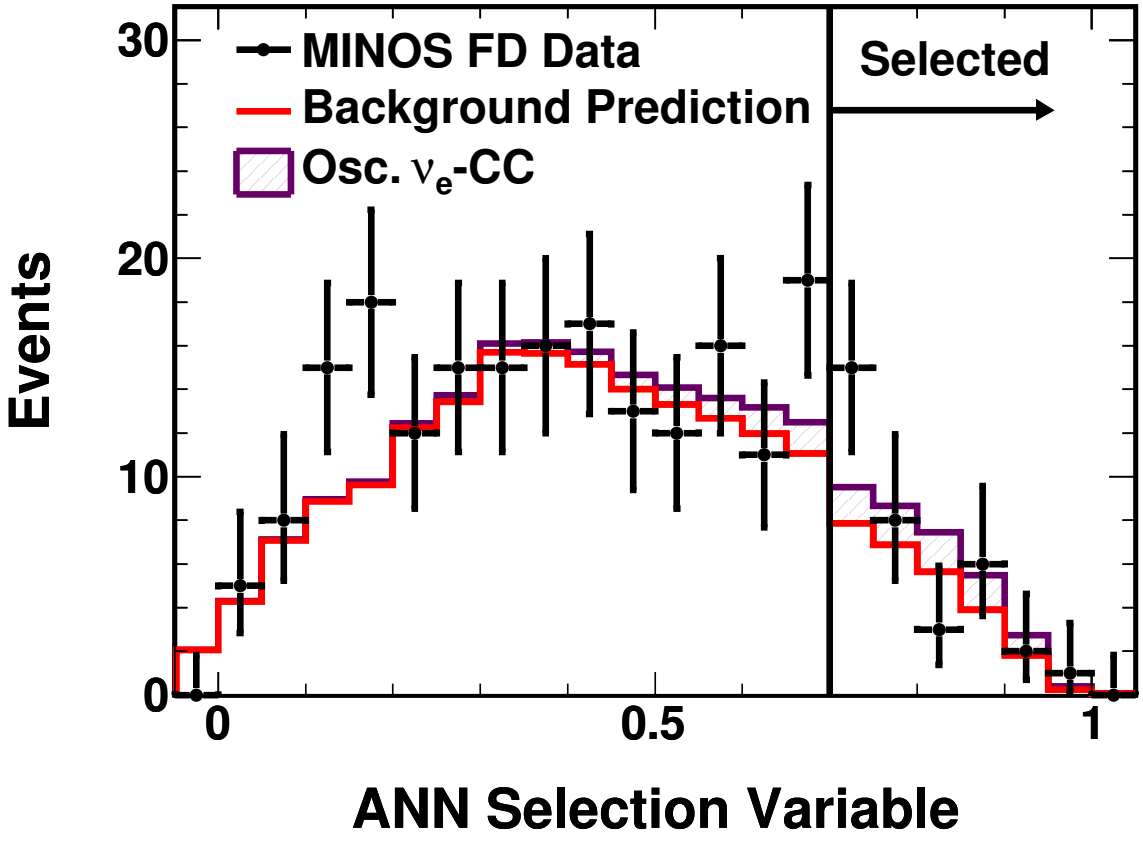

Figure 4: Distribution of the ANN selection variable for events in the FD. Black points show data with statistical error bars. The non-shaded histogram shows the background expectation. The shaded region shows the additional ν_e-CC events allowed from the best fit to the oscillation hypothesis as described in the text.

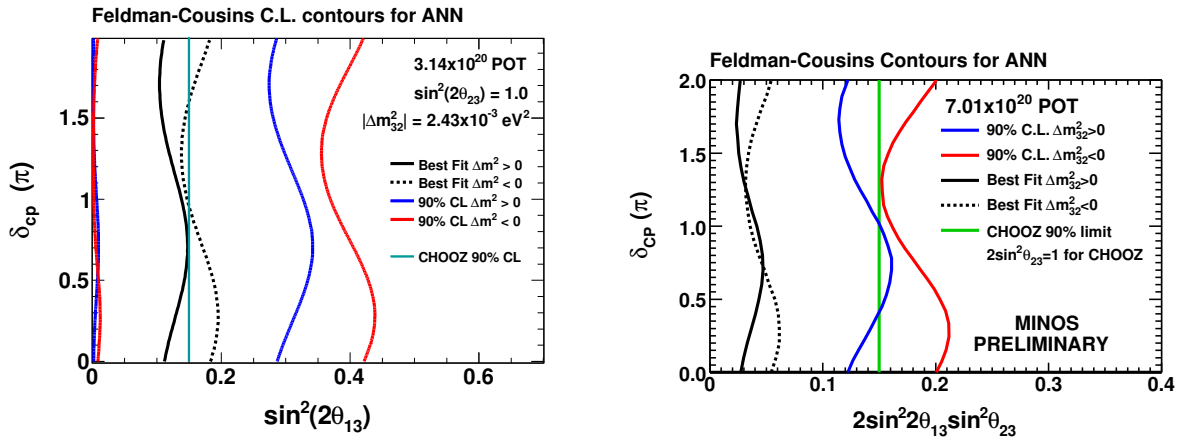

(a) 3.14×10^{20} POT

(b) 7.01×10^{20} POT

Figure 5: Values of $\sin^2(2\theta_{13})$ and δ_{CP} that produce a number of events consistent with the observation. Black lines show the best fit to the data for both the normal hierarchy (solid) and inverted hierarchy (dotted). Blue (red) curves show the 90% C.L. intervals for the normal (inverted) hierarchy. The CHOOZ limit is drawn for $\Delta m^2_{32} = 2.43 \times 10^{-3}$ eV^2 and $\sin^2(2\theta_{23}) = 1.0$. (a) Contours for 3.14×10^{20} POT; (b) Contours for 7.01×10^{20} POT. $\sin^2(2\theta_{23})$ is fixed at 1 in (a).

In the updated MINOS ν_e analysis based on 7.01×10^{20} POT data [12], there are many improvements. The improved crosstalk modeling was used in the simulation. The modeling of hadron intranuclear rescattering was improved by tuning the hadron-nucleus scattering cross section against external data. The effects caused by the variation of the neutrino beam intensity are properly modeled in the simulation. The shower reconstruction algorithm was refined to only use hits above a threshold of 2 photoelectrons. The ANN was re-optimized over a sample of simulated events generated with improved simulation and event reconstruction [26]. A third beam configuration was added in the ND background decomposition method where the hadron production target is moved upstream from the horns causing higher energy hadrons to be focused and yielding a neutrino spectrum peaked at 9 GeV. For the 7.01×10^{20} POT data sample we observe 54 events in the FD with an expected background of $49 \pm 7(\text{stat}) \pm 3(\text{syst})$, a 0.7 σ excess over the expected background. Figure 5(b) shows the resulting contours. The upper limits are $\sin^2(2\theta_{13}) < 0.12$ (0.20) at the 90% C.L. at $\delta_{CP} = 0$ for the normal (inverted) hierarchy.

7 Conclusions

We have reviewed the main techniques developed for the MINOS ν_e appearance search. MINOS is the first experiment to probe the unknown neutrino mixing angle θ_{13} beyond the CHOOZ limit. The current results represent the best constraint on the value of θ_{13} for nearly all values of δ_{CP} assuming the normal mass hierarchy and maximal $\sin^2(2\theta_{23})$. Currently a lot of efforts to further improve the results are under way.

Acknowledgments

This work was supported by the US DOE; the UK STFC; the US NSF; the State and University of Minnesota; the University of Athens, Greece; and Brazil's FAPESP, CNPq, and CAPES. We are grateful to the Minnesota DNR, the crew of the Soudan Underground Laboratory, and the staff of Fermilab for their contributions to this effort.

References

[1] Y. Ashie *et al.* (Super-Kamiokande Collaboration), Phys. Rev. Lett. **93**, 101801 (2004); Phys. Rev. D **71**, 112005 (2005).

[2] W. W. M. Allison *et al.* (Soudan-2 Collaboration), Phys. Rev. D **72**, 052005 (2005).

[3] M. Ambrosio *et al.* (MACRO Collaboration), Eur. Phys. J. C **36**, 323 (2004).

[4] M. H. Ahn *et al.* (K2K Collaboration), Phys. Rev. D **74**, 072003 (2006).

[5] B. Aharmim *et al.* (SNO Collaboration), Phys. Rev. C **72**, 055502 (2005).

[6] T. Araki *et al.* (KamLAND Collaboration), Phys. Rev. Lett. **94**, 081801 (2005).

[7] P. Adamson *et al.* (MINOS Collaboration), Phys. Rev. Lett. **101**, 131802 (2008).

[8] The experiment measures an unresolved mixture of $|\Delta m^2_{31}|$ and $|\Delta m^2_{32}|$ which we refer to as $|\Delta m^2|$ for brevity. For further discussion see G. Fogli *et al.*, Prog. Part. Nucl. Phys. **57**, 742 (2006).

[9] B. Pontecorvo, JETP **34**, 172 (1958); V. N. Gribov and B. Pontecorvo, Phys. Lett. **B28**, 493 (1969); Z. Maki, M. Nakagawa, and S. Sakata, Prog. Theor. Phys. **28**, 870 (1962).

[10] M. Apollonio *et al.* (CHOOZ Collaboration), Eur. Phys. J. C **27**, 331 (2003).

[11] P. Adamson *et al.* (MINOS Collaboration), Phys. Rev. Lett. **103**, 261802 (2009).

[12] P. Adamson *et al.* (MINOS Collaboration), Phys. Rev. D **82**, 051102 (2010).

[13] P. Adamson *et al.* (MINOS Collaboration), Phys. Rev. D **77**, 072002 (2008).

[14] D. G. Michael *et al.* (MINOS Collaboration), Nucl. Instrum. Meth. A **596**, 190 (2008).

[15] N. Tagg *et al.*, Nucl. Instrum. Meth. A **539**, 668 (2005).

[16] K. Lang *et al.*, Nucl. Instrum. Meth. A **545**, 852 (2005).

[17] R. Brun *et al.*, CERN Program Library W5013 (1984).

[18] A. Fasso *et al.*, CERN-2005-10, INFN/TC05/11, SLAC-R-773 (2005).

[19] H. Gallagher, arXiv:0806.2119 (2008).

[20] T. Yang, C. Andreopoulos, H. Gallagher, K. Hoffmann, and P. Kehayias, Eur. Phys. J. C **63**, 1 (2009).

[21] Z. Koba, H. B. Nielsen, and P. Olesen, Nucl. Phys. B **40** (1972) 317.

[22] T. Sjostrand, S. Mrenna, and P. Z. Skands, JHEP **0605**, 026 (2006).

[23] T. Yang, Ph.D. Thesis, Stanford University (2009).

[24] J. Boehm, Ph.D. Thesis, Harvard University (2009).

[25] A. Holin, Ph.D. Thesis, UCL (2010).

[26] J. Ling, Ph.D. Thesis, University of South Carolina (2010).

[27] J.P. Ochoa, Ph.D. Thesis, California Institute of Technology (2009).